RESEARCH ARTICLE

High Uptake and Fast Transportation of $LiPF_6$ in Porous Aromatic Framework for All-Solid-State Li-Ion Battery

Junyan Zou,[a] Abbie Trewin,[b] Teng Ben,*[a] and Shilun Qiu[a]

Abstract: All-solid-state Li-ion batteries (SSLIBs) have recently attracted substantial attention from scientists for the advantages of better safety performance. However, there are still several key challenges in SSLIBs that need to be addressed, such as low energy density, poor thermal stability or cycle stability, and large interface resistance. This contribution introduces a novel SSLIB with a porous aromatic framework (PAF-1) accommodating $LiPF_6$ that was used as the solid-state electrolyte (SSE) replacing the liquid electrolyte and diaphragm of traditional Li-ion batteries. The charge, discharge capacity, rate performance and cycle stability of the SSLIB were remarkably enhanced.

Introduction

With rising energy demand and urgency for energy storage, energy supply devices have become one of the critical priorities in modern society.[1-2] The well-developed preparation methodology extends traditional Li-ion batteries to be widely used in portable electronic devices. Compared with the traditional liquid Li-ion batteries, the solid-state Li-ion batteries (SSLIBs) have the advantages of better safety performance because the organic electrolyte is replaced by nonflammable solid-state electrolyte (SSEs).[3] SSLIBs can be classified as inorganic solid electrolyte batteries and polymer batteries depending on the SSE used. At present, inorganic solid electrolytes are mainly composed of oxides and sulfide solids, which have the advantage of high ionic conductivity. [3-4] However, there are still several key challenges in SSLIBs that need to be addressed, such as low energy density, poor thermal stability or cycle stability, and large interface resistance. Despite recent progress on reducing the interface resistance between the electrolyte and the electrode interface,[5-14] high performance SSLIB in terms of high energy density, excellent rate performance and long cycle life remain a challenge[3] because of the low uptake and slow transportation of Li-ion in SSE. Common materials, such as linear polymers, are difficult to meet these challenges due to their limited intermolecular free volume for Li^+ storage and transportation.[3, 5, 9, 15, 16]

To achieve the targeted high energy density and fast charge/discharge in “SSE”, an ideal material should play the role of high-uptake, directional, stable and fast transport of solvent-free electrolytes. Ultrahigh surface area porous polymer materials meet these requirements precisely because of their natural channels for ion transport. Among those porous materials reported to date which have surface area surpassing 5000 m^2g^{-1}, tetraphenyl methane linked 3D network, porous aromatic framework (PAF-1),[17] show very high physicochemical stability. Herein we introduce a porous polymer SSE which is composed of PAF-1 and the adsorbed lithium salt ($LiPF_6$) inside the aromatic channel. PAF-1 was synthesized as stated in our previous report.[17] Such SSE showed high uptake of lithium salt and high stability which endows the SSLIB with high energy density, long cycle life and excellent rate performance.

Results and Discussion

The porous polymer SSE was prepared by mixing the $LiPF_6$ and PAF-1 in a glove box in the mixed solution of ethylene carbonate (EC), dimethyl carbonate (DMC) and ethyl methyl carbonate (EMC) (1:1:1) (The concentration of $LiPF_6$ in the solvent is 1 M). The mud-like mixture was filtered and excess lithium salt was washed away by 1:1:1 mixture of EC/EMC/DMC. After drying under vacuum to remove excess solvents from the solid material, the resulting $LiPF_6$@PAF-1 (4.8 g g^{-1}) was obtained as a light brown powder. FT-IR indicated that a high boiling point EC was also included inside the pores of PAF-1 (Figure S1). The amount of $LiPF_6$ in $LiPF_6$@PAF-1 was determined by Inductively Coupled Plasma (ICP) analysis. A series of $LiPF_6$@PAF-1 SSE with different $LiPF_6$ loading amount (15.6 – 40.8 wt%, See supporting information section 1) were prepared and conductivity were measured by AC impedance. The optimized $LiPF_6$@PAF-1 ($LiPF_6$ = 33.0 wt%) showed the highest bulk conductivity of 4.0 x 10^{-4} Scm^{-1} and were selected for further study (Figure S2 and Table S2).

Observed from the X-ray diffraction pattern (Figure S3), $LiPF_6$@PAF-1 was amorphous in nature, which was beneficial as an isotropic electrolyte for SSLIBs. The thermogravimetric analysis (TGA) plot (Figure S4) showed a significant decline from 360 K. It should be noted that the decomposition temperature of $LiPF_6$ is about 333 K,[18] which revealed that lithium salt was stabilized in the PAF-1 aromatic channel. The differential scanning calorimetry analysis (Figure S5) indicated that no endothermic peak could be found before the decomposition temperature (360 K) of the $LiPF_6$@PAF-1 and the glass-transition temperature (Tg) of PAF-1 was about 427 K.

The binding energies of Li^+ and PF_6^- to a fragment of the PAF-1 material were calculated using density functional theory (DFT) with Gaussian to understand this stabilization effect of PAF-1 on the $LiPF_6$ salt. The B3LYP functional was used with the 6-311+g(d) basis set. Both Li^+ and PF_6^- are stabilized by the PAF-1 fragment with binding energies of -390 kJ mol^{-1} and -192 kJ mol^{-1} respectively compared to the respective gas phase ions (Table S1). The Li^+ is located between two phenyl rings of the tetra

[a] J. Zou, Prof. T. Ben, Prof. S. Qiu
Department of Chemistry, Jilin University
130012 Changchun (China)
E-mail: tben@jlu.edu.cn
[b] Prof. A. Trewin
Department of Chemistry, Lancaster University
Bailrigg, Lancaster, LA1 4YB (UK)

Supporting information for this article is given via a link at the end of the document.

phenyl methane node of the PAF-1 structure (Figure 1, Figure S6, S7). This is a similar location to that observed for Li^+ adsorbed on a single benzene ring but here we have the additional benefit of being able to interact with two phenyl rings simultaneously, which proves that the Li^+ is stabilized by aromatic channel of PAF-1. This can be explained by the so-called Cation-π interaction between Li^+ and aromatic ring.[19-22] Further binding energy calculations reveal that it is more energetically favorable for the Li^+ and PF_6^- to bind together to the PAF-1 fragment with a binding energy of -246 kJ mol^{-1} compared to gas phase $LiPF_6$. It is favorable to further consecutively bind two, three and four $LiPF_6$ units to the PAF-1 fragment with binding energies of -61 kJ mol^{-1}, -67kJ mol^{-1} and -71 kJ mol^{-1} respectively.

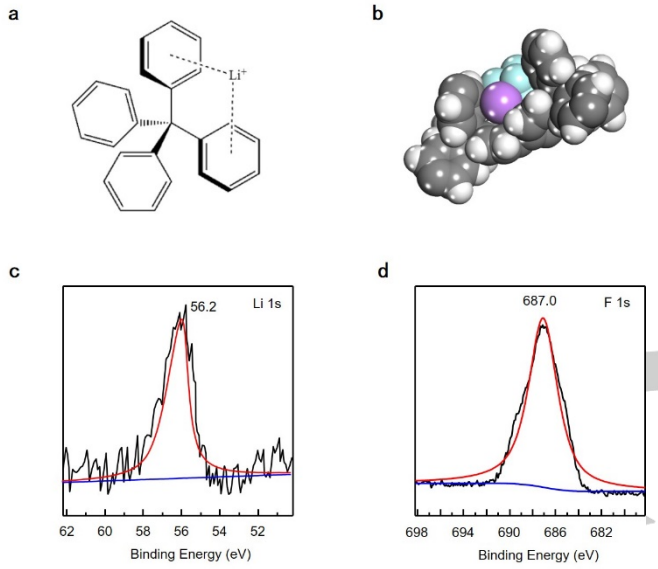

Figure 1. (a) Schematic showing the interaction of the Li^+ ion with the faces of the two phenyl rings of the tetra phenyl methane nodes of PAF-1. (b) The van der Waals radius of each respective atom, Li ions are coloured purple while F, P, C and H atoms are coloured light blue, pink, grey and white, respectively. (c) XPS Li 1s and (d) F 1s spectrum of $LiPF_6$@PAF-1.

In order to understand the high uptake and stabilization effect of $LiPF_6$ in the pore channels of PAF-1, the theoretical capacity of $LiPF_6$ in a PAF-1 model was calculated using simulated annealing within the *Sorption* module of the Materials Studio Package using the PCFF force field.[23] The PAF-1 model structure was generated by topological mapping to a model of amorphous silica, (Figure S8), as described in previous publication.[24] The PAF-1 model is a representative sample of the amorphous structure as it has a large unit cell (74 Å × 74 Å × 74 Å) and so artificial crystallinity is minimized.

The maximum capacity obtained was 735 $LiPF_6$ per unit cell (74 Å × 74 Å × 74 Å) of the PAF-1 model (Figure S9), indicating that the microporous regions of PAF-1 have a high $LiPF_6$ capacity, which when added to uptake contributions from the meso- and macro-porous regions accounts for the high uptake capacity observed for PAF-1. The most favorable location for the adsorption of the $LiPF_6$ is with the Li^+ sitting between two phenyl rings, similarly to the binding site calculated using DFT, shown in Figure 1.

X-ray photoelectron spectroscopy (XPS) analysis of Li 1s and F 1s of $LiPF_6$@PAF-1 SSE are shown in Figure 1c and d, respectively. Compared with $LiPF_6$ crystal,[25] the binding energy of both Li 1s and F 1s were changed to 56.2 and 687.0 eV, indicating strong interaction between $LiPF_6$ and PAF-1 framework.

The PF_6^- ion is large and as such is the limiting factor in the ability of the PAF-1 structure to uptake $LiPF_6$. To probe the accessibility of the PAF-1 structure for PF_6^-, a geometric surface was calculated for a probe radius of 3.7 Å, the radius of a PF_6^- ion. Figure S10 shows the calculated Connolly surface that extends throughout the PAF-1 structure showing that the PAF-1 structure is fully accessible to PF_6^-. To test the ability of the PF_6^- ion to diffuse through the PAF-1 structure, we have run molecular dynamic simulations using the DL Poly computational code. A PF_6^- ion was placed within the PAF-1 structure and its diffusion at 398 K monitored. The trajectory is shown in Figure S11 and shows that the PF_6^- ion is able to diffuse freely through the PAF-1 structure.

The PF_6^- ion must be able to diffuse freely when under the presence of a charge bias without disrupting the PAF-1 structure. A cluster of PAF-1 is placed between two graphene sheets with z values of ~ 1 Å and 79 Å that will act as the respective anode and cathode. A PF_6^- ion is placed with a z value of ~ 75 Å. The cathode and anode graphene sheets are charged +0.16 e and -0.16 e respectively. This charge is based on a surface charge density s = 0.04 C m^{-2} of the electrode. It is calculated from the formula: q = s/r, where r is the surface density of carbon atoms of the graphene electrode. During the molecular dynamics simulation, the PF_6^- ion will diffuse away from the anode towards the cathode via the most direct route possible for that starting position. Figure S12 shows the trajectory of the PF_6^- ion and a plot of the z value versus the simulation time. This was repeated 4 times with the PF_6^- ions in different starting positions (Figure S13). In each case the PF_6^- ion was able to diffuse easily to the cathode via a direct path with little interaction with the PAF-1 structure.

The ease of the active diffusion of PF_6^- ion within our simulations, which are rigid and therefore do not allow any rearrangement that would aid diffusion, suggests that the diffusion of the PF_6^- ion within the real system is facile and does not require any rearrangement of the PAF-1 material. This accounts for the relative robustness of the PAF-1 material to the diffusion of the ions through the PAF-1 network.

$LiPF_6$ is physically adsorbed inside PAF-1 though there are strong binding between $LiPF_6$ and PAF-1 frameworks. However, PAF-1 could be easily recovered by exchange with ethyl alcohol several times. EDS of recovered PAF-1 showed almost no signal of F and P (Figure S14).

^7Li, ^{19}F, and ^{31}P MAS solid-state nuclear magnetic resonance (ssNMR) of $LiPF_6$@PAF-1 at 298 K are shown in Figure S15, indicating uniform distribution and chemical environment of $LiPF_6$ in pores of PAF-1. The variable temperatures of static SPE ssNMR was applied to explore the mobility of Li^+ (Figure 2a) and PF_6^- (Figure 2b) in $LiPF_6$@PAF-1 SSE. Singlet of $^7Li^+$ and doublet of ^{19}F was observed at 273 K in SPE ssNMR, respectively. With the increase of the temperature, a noticeable narrowing of the width of the ^7Li signal can be observed which resulted from the high mobility of Li^+ ions that attenuate the ^7Li quadrupole coupling

and the ^{1}H-^{7}Li dipolar coupling.[26] In the case of ^{19}F, the width change

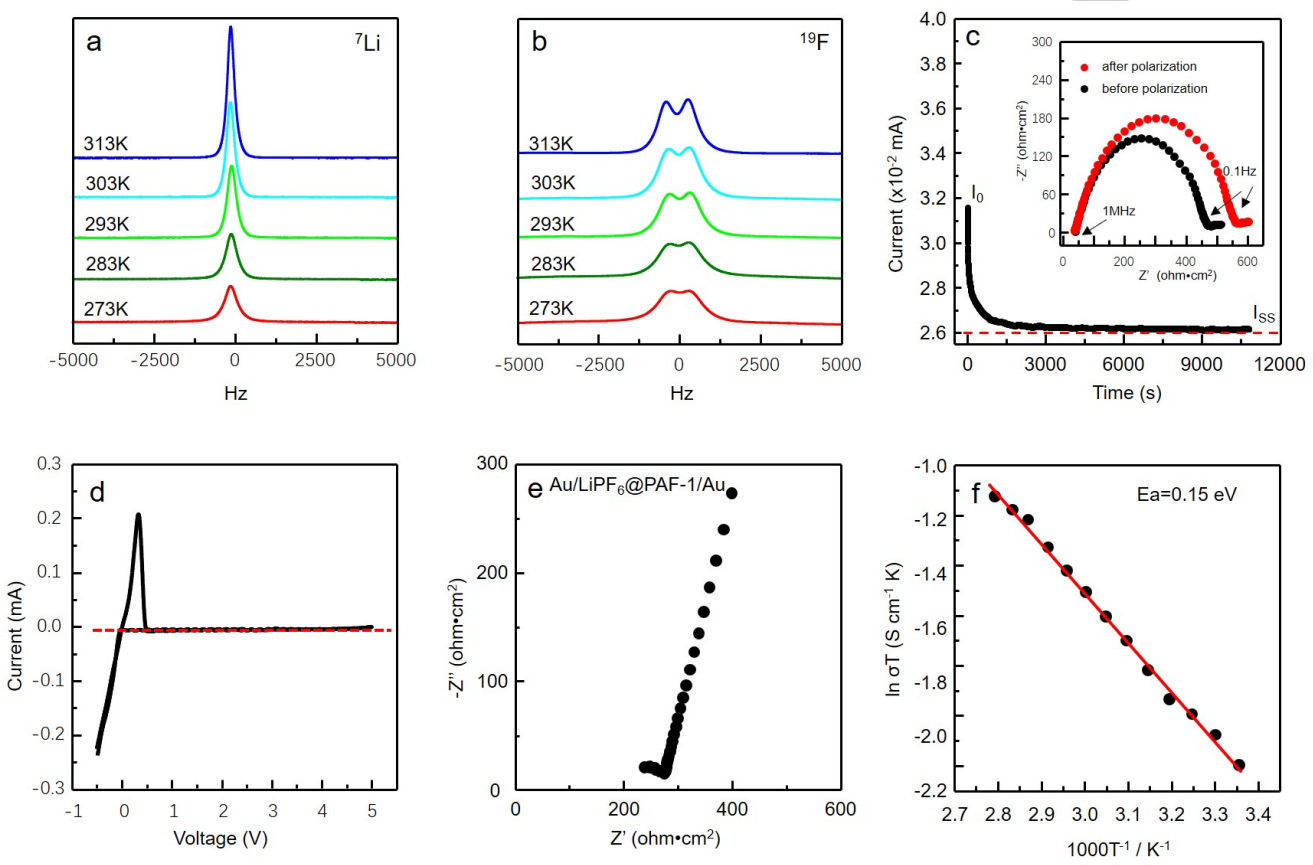

Figure 2. Properties of $LiPF_6$@PAF-1 electrolyte. (a) The ^{7}Li and (b) the ^{19}F static SPE ssNMR spectra of $LiPF_6$@PAF-1 from 273 K to 313 K. (c) Lithium-ion transference number measurement of the $LiPF_6$@PAF-1. Polarization curve of Li‖$LiPF_6$@PAF-1‖Li Cell and the inset is AC impedance plots before and after polarization. (d) CV curve of the Li‖$LiPF_6$@PAF-1‖Stainless steel cell with a scan rate of 0.2 mV s^{-1}. (e) Nyquist plots of $LiPF_6$@PAF-1 at 298 K. (f) Arrhenius plot showing the Li-ion conduction from 298 K to 358 K.

of the signal is not as significant as that of Lithium, indicating that the mobility of PF_6^- in the pores of PAF-1 is weaker than that of Li^+, which is in accordance with the results of molecular dynamics simulation.

Figure 2c shows the Lithium-ion transference number (t_{Li+}) of $LiPF_6$@PAF-1 at 298 K by means of DC polarization and AC impedance measurements of lithium symmetric coin-type cell (Li‖$LiPF_6$@PAF-1‖Li, Supporting information, Section 3.2).[27] When the cell is subjected to a very low polarization voltage (Δ_V = 10 mV), the current was found to fall from its initial value (I_0) to a steady state value (I_{ss}). In this case, the contribution of the current was only coming from the transportation of Li^+. The inset in Figure 2c shows the Nyquist plots of the lithium symmetric coin-type cells before and after polarization and the resistances are 431 ohm•cm^2 and 522 ohm•cm^2, respectively. The t_{Li+} was then calculated as high as 0.859, indicating the ionic conductivity was mostly contributed by the Li^+.

Cyclic voltammogram (CV) of the Li‖$LiPF_6$@PAF-1‖stainless steel coin-type cell was measured at 298 K to determine the electrochemical working window with a scan rate of 0.2 mVs^{-1} at -0.5 and 5.0 V (Figure 2d). Symmetric peaks of lithium deposition and dissolution was observed at about 0 V,[28] while no obvious redox signals can be detected in the scanned voltage range until 4.9 V, which shows the ultrahigh electrochemical stability of the $LiPF_6$@PAF-1 SSE.

The bulk resistance, grain boundary resistance, and double layer capacitance from ion blocking electrodes were determined by electrochemical impedance spectroscopy. A typical Nyquist plot of a dense $LiPF_6$@PAF-1 SSE was shown in Figure 2e, and the bulk resistance and total resistance was calculated to be 251 ohm•cm^2 and 268 ohm•cm^2, respectively. Figure 2f showed the Arrhenius plot of the SSE measured at different temperatures. The conductivities exhibit an appearance increase with increasing temperature, (Figure S16) illustrating the faster movement of Li^+ and PF_6^- at higher temperature in the pores of PAF-1, which is in accordance with the observations of ssNMR.

CR2032 coin-type cells were assembled in an argon-filled glove box shown in Figure 3a. A typical procedure for cell set-up was to first place the cathode shell openings followed by placing the $LiFePO_4$ cathode layer in the middle of the cathode shell with

the coating facing up. Successive layers included the SSE layer ($LiPF_6$@PAF-1), anode layer (lithium plate), current collector layer (stainless steel), respectively. Finally, the anode shell was clamped with tweezers to cover and buckle the whole battery. To

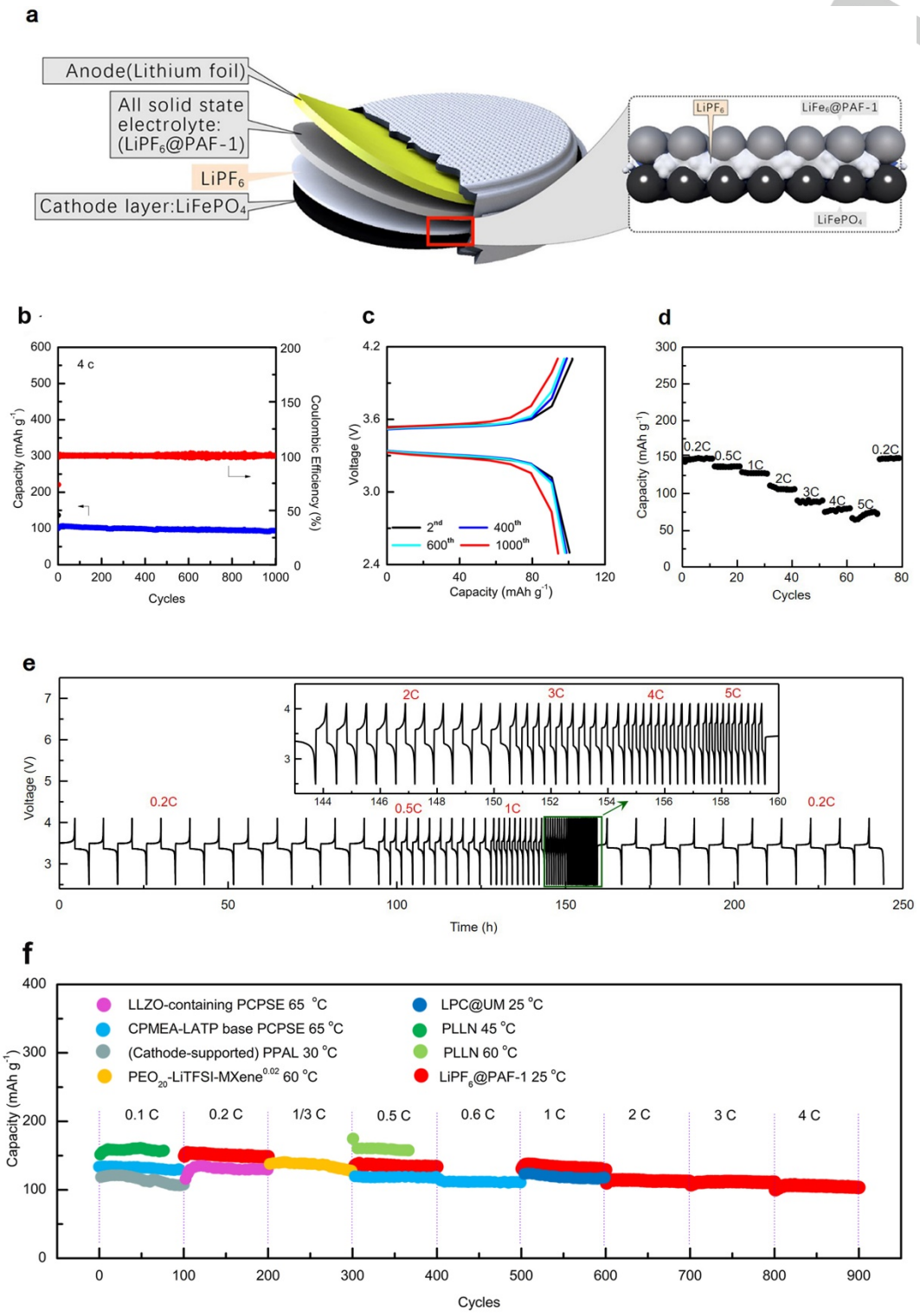

Figure 3. Schematic and characterization of the $LiFePO_4$‖$LiPF_6$@PAF-1‖Li cell. (a) Schematic diagram for the $LiFePO_4$‖$LiPF_6$@PAF-1‖Li cell. (b) AC impedance spectrum of the $LiFePO_4$‖$LiPF_6$@PAF-1‖Li cell before circulation. (c) Cycling stability and Coulombic efficiency of the $LiFePO_4$‖$LiPF_6$@PAF-1‖Li cell at a current density of 4C, inset is the Voltage profiles. (d) Rate capabilities of the $LiFePO_4$‖$LiPF_6$@PAF-1‖Li cell. (e) Voltage profiles versus time of $LiFePO_4$‖$LiPF_6$@PAF-1‖Li

cell at different current density. (f) Cycling performance of Li/$LiFePO_4$ cells with other SSEs and $LiPF_6$@PAF-1 in long term cycles (first 100 cycles). (LLZO-containing PCPSE[5], CPMEA-LATP base PCPSE[5], Cathode-supported PPAL[9], PEO_{20}-LiTFSI-MXene$^{0.02}$[16], LPC@UM[31], PLLN[32].)

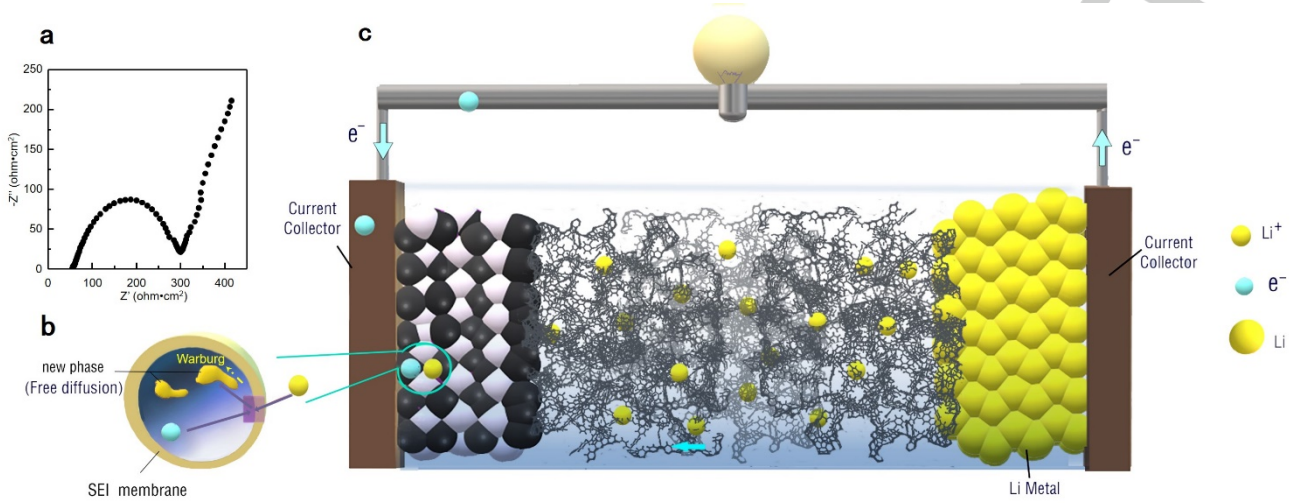

Figure 4. Mechanism of operation of the $LiFePO_4$‖$LiPF_6$@PAF-1‖Li cell.

fabricate the SSLIB with better properties, lower interfacial resistance was required. For garnet-electrolyte based SSLIB, an interphase between SSE and anode were introduced to enhance the contact and therefore to reduce the interfacial resistance.[6, 10, 13] While for the polymer type SSE, a simple wetting method has been reported recently and the interfacial resistance could be reduced effectively.[9] In our case, two droplets (ca. 55 μL) of $LiPF_6$ electrolyte (1 M $LiPF_6$ in a mixture of ethylene carbonate, dimethyl carbonate and ethyl methyl carbonate in the volume ratio of (1:1:1)) was dropped on the surface of the cathode and anode layer and then fully dried. To verify the enhancement of the interfacial contact by droplet of $LiPF_6$ solution in anode, dense $LiPF_6$@PAF-1 pellet was sandwiched between two Lithium foils with droplet treatment to set up a symmetric cell for the measurement of Li/$LiPF_6$@PAF-1 interfacial resistance.[6] As a control experiment, the symmetric cell without droplet treatment was also fabricated by same condition. The interfacial resistance of the symmetric cell treated by droplet of $LiPF_6$ solution is about 39 ohm•cm^2, which is much lower than that without treatment (Figure S17). These phenomena can also be confirmed by the observation of total resistance change of $LiFePO_4$‖$LiPF_6$@PAF-1‖Li coin-type cell. The total resistance was reduced to 300 ohm•cm^2 after the cathode was treated with a droplet of $LiPF_6$ solution (Figure S18).

Figure S19 showed the cross-sectional SEM image of the cathode. No significant delamination phenomenon was observed which indicated that $LiPF_6$ was uniformly embedded in the gap between the $LiFePO_4$ spherical particles. This architecture was beneficial to the tight contact between cathode layer and SSE, hence effectively reducing the interface resistance.

Cycling performance, charge and discharge voltage profiles of the $LiFePO_4$‖$LiPF_6$@PAF-1‖Li cell at the current density of 4C were shown in Figure 3b and 3c. After thousands of cycles, the capacity of the battery was maintained at a constant value of 94.2 mAh g^{-1}, and the coulomb efficiency was kept close to 100%. This battery also performed well at other current densities of 0.2, 0.5, 1, 2, and 3 C (See supporting information Figure S20 - 24), which suggested that the ultrahigh stability of the $LiFePO_4$‖$LiPF_6$@PAF-1‖Li cell was achieved both in long time cycle and high current density.

A robust rate performance was shown in Figure 3d. The $LiFePO_4$‖$LiPF_6$@PAF-1‖Li cell charged and discharged at a rate of 0.2C first, then gradually increased to 5C, while maintaining 10 cycles at each rate. At the current density of 0.2C, discharge capacity of the battery was about 148 mAh g^{-1}. When higher current densities (0.5C, 1C, 2C, 3C, 4C, 5C) were applied, the capacity of the battery is maintained above 80% compared with the corresponding capacity of the previous rate. When the current density was switched back to 0.2C, a capacity of 148 mAh g^{-1} is recovered. These results showed that the $LiFePO_4$‖$LiPF_6$@PAF-1‖Li cell have superior performance in the wide current range and were suitable for the high rate application of Li-ion batteries.[29-30] The voltage versus time profiles of the battery under each current density corresponding to the rate capacity test were shown in Figure 3e. The voltage profiles were very stable, and there was no obvious fluctuation under different current densities, indicating good circularity and stable interface of the battery.[7] Figure 3f further compares the cycling performance $LiFePO_4$‖$LiPF_6$@PAF-1‖Li cell and other SSLIBs [5, 9, 16, 31, 32] that have been well studied. $LiFePO_4$‖$LiPF_6$@PAF-1‖Li cell exhibits high capacity with robust electrochemical stability and importantly, it sustained rigorous long-term current density as high as 4C.

In order to further explore the ionic conduction mechanism of the $LiFePO_4$‖$LiPF_6$@PAF-1‖Li cell, the battery was characterized

by AC impedance Spectroscopy (Figure 4a).[33-35] The first semicircle of the Nyquist plot in the high frequency region represents the resistance of lithium ions migrating through the surface film of the active material particles, coupled with film capacitance (Figure 4b).[33-36] Figure 4c showed a schematic diagram of $LiFePO_4$‖$LiPF_6$@PAF-1‖Li cell. The anode material was lithium metal. When the battery was working, the lithium atoms lost electrons and was oxidized to lithium ions. The lithium ions were transferred to the cathode via the SSE, combined with electrons from the external circuit, and then reduced to lithium atoms. In this process, the external circuit received current and was energized.[32]

To test the ability of Li^+ to diffuse through the PAF-1 material, the active diffusion of a Li^+ ion through a PAF-1 cluster is simulated using molecular dynamic simulation. The Li^+ is positioned with a z value of approximately 5 Å, close to the positively charged graphene sheet. This is repeated for a further three lithium ions. The Li^+ diffuses towards the negatively charged graphene sheet but for each ion the active diffusion ceases after 5-8 Å, shown in Figure S25, S26. Assessment of the trajectories reveals that each Li^+ is attracted to the first phenyl ring that is in its pathway and moves to the high energy binding site located between two phenyl rings identified through DFT calculation and simulated annealing. In the fully loaded $LiPF_6$@PAF-1 system, we therefore expect that the high energy binding sites will be fully occupied by $LiPF_6$. The Li^+ diffusion must therefore occur via more loosely bound Li^+ ions that fill the remaining void space. To test this, the Connolly surface area of the PAF-1 model fully loaded with 735 $LiPF_6$ was calculated using a probe radius of 0.76 Å, the ionic radius of Li^+. The calculated Connolly surface area, shown in Figure S27, extends throughout the system showing that there is clear pore volume for Li^+ diffusion pathways.

Conclusion

In conclusion, we have used a porous polymer, namely, PAF-1 as the matrix enclosing $LiPF_6$ inside that was used as the electrolyte instead of the liquid electrolyte and diaphragm of traditional Li-ion batteries. Theoretical calculations revealed high binding energy between Li^+ and PAF-1 aromatic frameworks. Moreover, after binding with Li^+, PAF-1 still have high enough pore volume for fast Li^+ transportation, which was confirmed by ssNMR, and AC impedance spectra. $LiPF_6$@PAF-1 also exhibits high electrochemical stability and can be used as a solid-state electrolyte. Hence the $LiFePO_4$‖$LiPF_6$@PAF-1‖Li all-solid-state Li-ion batteries developed exhibit outstanding electrochemical performance in terms of charge, discharge capacity and cycle stability at low current densities as well as under high current densities. Thus, The $LiFePO_4$‖$LiPF_6$@PAF-1‖Li pave the way to extend the usage of porous organic polymers as potential high energy density solid-state electrolyte materials in electrochemistry.

Experimental Section

Experimental details can be found in the Supporting Information.

Acknowledgements

This study was supported by the National Natural Science Foundation of China (No. 21871103) and the Science and Technology Department of Jilin Province Foundation (20180414009GH).

Keywords: All-Solid-State • Conducting materials • Electrochemistry • Li-ion Battery • Porous Aromatic Framework

[1] P. Geng, S. Zheng, H. Tang, R. Zhu, L. Zhang, S. Cao, H. Xue, H. Pang, *Adv. Energy Mater.* **2018,** *8*, 1703259.
[2] J. M. Tarascon, M. Armand, *Nature.* **2001,** *414*, 359-367.
[3] A. Manthiram, X. Yu, S. Wang, *Nat. Rev. Mater.* **2017,** *2,* 16103.
[4] N. Kamaya, K. Homma, Y. Yamakawa, M. Hirayama, R. Kanno, M. Yonemura, T. Kamiyama, Y. Kato, S. Hama, K. Kavamoto, A. Mitsui, *Nat. Mater.* **2011,** *10*, 682-686.
[5] W. Zhou, S. Wang, Y. Li, S. Xin, A. Manthiram, J.B. Goodenough, *J. Am. Chem. Soc.* **2016,** *138*, 9385−9388.
[6] W. Luo, Y. Gong, Y. Zhu, K. K. Fu, J. Dai, S. D. Lacey, Wang, C. B. Liu, X. Han, Y. Mo, E. D. Wachsman, L. Hu, *J. Am. Chem. Soc.* **2016,** *138*, 12258−12262.
[7] J. Broek, S. Afyon, J. L. M. Rupp, *Adv. Energy Mater.* **2016,** *6*, 1600736.
[8] K. Fu, Y. Gong, G. T. Hitz, D. W. McOwen, Y. Li, S. Xu, Y. Wen, L. Zhang, C. Wang, G. Pastel, J. Dai, B. Liu, H. Xie, Y. Yao, E. D. Wachsman, L. Hu, *Energy Environ. Sci.* **2017,** *10*, 1568-1575.
[9] X. Chen, W. He, L. X. Ding, S. Wang, H. Wang, *Energy Environ. Sci.* **2019.** *12,* 938-944.
[10] K. Fu, Y. Gong, B. Liu, Y. Zhu, S. Xu, Y. Yao, W. Luo, C. Wang, S. D. Lacey, J. Dai, Y. Chen, Y. Mo, E. Wachsman, L. Hu, *Sci. Adv.* **2017.** *3*, e1601659.
[11] Y. Kato, S. Hori, T. Saito, K. Suzuki, M. Hirayama, A. Mitsui, M. Yonemura, H. Iba, R. Kanno, *Nat. Energy.* **2016.** *1*, 16030.
[12] J. H. Woo, J. E. Trevey, A. S. Cavanagh, Y. S. Choi, S. C. Kim, S. M. George, K. H. Oh, S.H. Lee, *J. Electrochem. Soc.* **2012.** *159*, A1120-A1124.
[13] W. Luo, Y. Gong, Y. Zhu, Y. Li, Y. Yao, Y. Zhang, K. Fu, G. Pastel, C. F. Lin, Y. Mo, E. D. Wachsman, L. Hu, *Adv. Mater.* **2017.** *29*, 1606042.
[14] N. Ohta, K. Takada, L. Zhang, R. Ma, M. Osada, T. Sasaki, *Adv. Mater.* **2006.** *18*, 2226-2229.
[15] Z. Xue, D. He, X. Xie, *J. Mater. Chem. A.* **2015,** 3, 19218.
[16] Q. Pan, Y. Zheng, S. Kota, W. Huang, S. Wang, C. Y. Li, *Nanoscale Adv.* **2019.** 1, 395-402.
[17] T. Ben, H. Ren, S. Ma, D. Cao, J. Lan, X. Jing, W. Wang, F. Xu, J. Deng, M. Simmons, S. Qiu, G. Zhu, *Angew. Chem. Int. Ed.* **2009,** *48,* 9457-9460; *Angew. Chem.* **2009,** *121,* 9621-9624.
[18] B. Ravdel, K. M. Abraham, R. Gitzendanner, J. Dicarlo, B. Lucht, C. Campion, *J. Power Sources.* **2003,** *119-121,* 805-810.
[19] J. C. Ma, D. A. Dougherty, *Chem. Rev.* **1997,** *97,* 1303-1324.
[20] K. S. Kim, P. Tarakeshwar, J. Y. Lee, *Chem. Rev.* **2000,** *100,* 4145-4186.
[21] R. Amunugama, M. T. Rodgers, *In. J. Mass. Spec,* **2003,** *222,* 431-450.
[22] A. Mohajeri, E. Karimi, *J. Mol. Struct.* **2006,** *774,* 71-76.
[23] H. Sun, *Macromolecules.* **1995,** 28, 701-712.
[24] J. M. H. Thomas, A. Trewin, *J. Phys. Chem. C.* **2014,** *118*, 19712-19722.
[25] R. Dedryvère, S. Leroy, H. Martinez, F. Blanchard, D. Lemordant, D. Gonbeau, *J. Phys. Chem. B.* **2006,** 110, 12986-12992.
[26] X. Fu, L. Yang, J. Ma, G. Yang, Y. Yao, Q. Chen, *Polymer.* **2016,** 105, 310-317.
[27] P. Bruce, J. Evans, C. Vincent, *Solid State Ionics.* **1988,** 28-30, 918-922.
[28] T. Kasajima, T. Nishikiori, T. Nohira, Y. Ito, Electrochem. Solid. St. 2003, 6, E5-E9.
[29] Y. E. Miao, G. N. Zhu, H. Hou, Y. Y. Xia, T. Liu, *J. Power Sources* **2013,** *226,* 82-86.

[30] D. Lin, D. Zhuo, Y. Liu, Y. Cui, *J. Am. Chem. Soc.* **2016,** *138*, 11044−11050.
[31] L. Shen, H. W, F. Liu, J. L. Brosmer, G. Shen, X. Wang, J. I. Zink, Q. Xiao, M. Cai, G. Wang, Y. L, B. Dunn, *Adv. Mater.* **2018.** 30, 1707476.
[32] Z. Wan, D. Lei, W. Yang, C. Liu, K. Shi, X. Hao, L. Shen, W. Lv, B. Li, Q. Yang, F. Kang, Y. He, *Adv. Funct. Mater.* **2018.** 1805301, 1-10
[33] Q. Zhuang, X. Qiu, S. Xu, Y. Qiang, S. Sun in *Lithium Ion Batteries - New Developments*, Ch. 8 (Eds.: I. Belharouak), InTech, **2012**, pp 190-226.
[34] E. Barsoukov, J. H. Kim, D. H. Kim, K. S. Hwang, C. O. Yoon, H. Lee, *J. New. Mat. Electr. Sys.* **2000.** *3*, 301-308.
[35] N. Bonanos, B. C. H. Steele, E. P. Butler in *Impedance spectroscopy*, *Second Edition*, Ch. 4 (Eds.: E. Barsoukov, J. R. Macdonald), John Wiley & Sons, Inc., Hoboken, New Jersey, **2005**, pp. 205-530.
[36] S.S. Zhang, K. Xu, T. R. Jow, *Electrochim. Acta.* **2004,** 49, 1057-1061.

Entry for the Table of Contents (Please choose one layout)

Layout 1:

RESEARCH ARTICLE

A novel all-solid-state Li-ion battery with Porous Aromatic Framework accommodating $LiPF_6$ that was used as the solid-state electrolyte exhibit outstanding electrochemical performance in terms of charge, discharge capacity and cycle stability. Theoretical calculations revealed high binding energy between Li^+ and PAF-1. After binding with Li^+, PAF-1 still have high enough volume for Li^+ transportation.

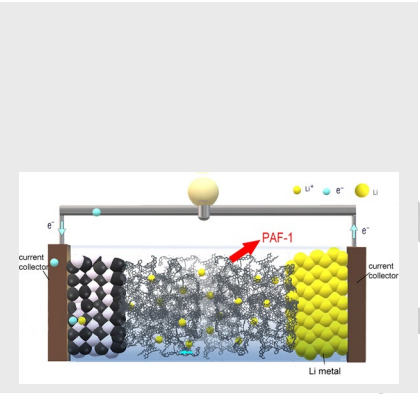

*Junyan Zou, Abbie Trewin, Teng Ben, * Shilun Qiu*

Page No. – Page No.

High Uptake and Fast Transportation of $LiPF_6$ in Porous Aromatic Framework for All-Solid-State Li-Ion Battery

Layout 2:

RESEARCH ARTICLE

((Insert TOC Graphic here))

*Author(s), Corresponding Author(s)**

Page No. – Page No.

Title

Text for Table of Contents